npj | quantum materials

Article

Published in partnership with Nanjing University

https://doi.org/10.1038/s41535-026-00909-0

Between Mott and cluster Mott: spin-orbit entangled dimer singlets in $Ba_3CeRu_2O_9$

Lara Pätzold[1], Anna Sandberg[2], Henrik Schilling[3], Hlynur Gretarsson[4], Enrico Bergamasco[1], Marco Magnaterra[1], Petra Becker[3], Paul H. M. van Loosdrecht[1], Jeroen van den Brink[5,6], Maria Hermanns[2,7] & Markus Grüninger[1] ✉

The hexagonal 4*d* ruthenates $Ba_3MRu_2O_9$ host structural dimers and exhibit a delicate balance of competing interactions. Hund's coupling, trigonal crystal-field splitting, and hopping for a_{1g} and e_g^π orbitals all fall within a narrow energy window. This yields a series of possible ground states, ranging from the localized Mott limit with (anti-)ferromagnetic exchange coupling via orbital-selective behavior to the cluster Mott limit with quasimolecular orbitals that are delocalized over the two dimer sites. Using resonant inelastic x-ray scattering, we show that $Ba_3CeRu_2O_9$ with four holes per dimer resides in the intricate crossover regime between the localized Mott case and the quasimolecular limit. The spin-orbit entangled singlet ground state predominantly shows a Mott-like charge distribution with two holes per Ru site, but at the same time a dominant fraction of the holes occupies bonding orbitals. Furthermore, spin and orbital occupation contradict an exchange-based Mott scenario but agree with a cluster Mott approach. A quasimolecular trial wave function describes more than 70 % of the ground state. In this crossover regime, small changes of, e.g., the crystal field may strongly affect the character of electronic states. In $Ba_3CeRu_2O_9$, both the crystal field and hopping lower the a_{1g} orbitals. For spin-orbit coupling $\zeta = 0$, Hund's coupling favors an $S = 0$ ground state for small hopping but $S = 1$ for realistic larger hopping. Finite ζ, even though small, finally yields a non-magnetic $J = 0$ state.

In correlated transition-metal compounds, the entanglement of spins and orbitals and their interplay with other degrees of freedom give rise to an intriguing variety of properties and phases[1–5]. The cornucopia of different crystal structures and substitutions offers the opportunity to realize different parameter regimes and to tune the material properties. A prominent example are compounds with $4d^4$ Ru^{4+} ions. The rich phase diagram of layered $Sr_{2-x}Ca_xRuO_4$ includes the highly controversial unconventional superconductivity in Sr_2RuO_4[6–8] and a temperature-driven metal-insulator transition and antiferromagnetic order in Ca_2RuO_4[9,10]. For intermediate x, an orbital-selective Mott transition has been discussed[2,11,12], where the degree of Mott localization depends on the orbital character. For well separated Ru ions as in cubic K_2RuCl_6, spin-orbit coupling ζ yields a nonmagnetic $J = 0$ ground state[13]. The competition of ζ and tetragonal crystal-field splitting Δ_{tet} has been discussed extensively in Ca_2RuO_4[14–21]. From the perspective of large Δ_{tet} lifting orbital degeneracy, Ca_2RuO_4 can be viewed as an $S = 1$ antiferromagnet in which ζ causes a large single-ion anisotropy[14,16]. The alternative scenario of excitonic magnetism[22] starts from large ζ and local $J = 0$ moments and considers condensation of a dispersive, magnetic excited state. In this case, one expects a longitudinal magnon that has been discussed as being equivalent to a Higgs mode[15]. In fact, the local $4d^4$ ground state is a $J = 0$ singlet for any Δ_{tet}/ζ, and sizable Δ_{tet} facilitates condensation in this picture.

Novel states of quantum matter may be realized in cluster Mott insulators[2,3,23–26], which in essence are located in between Mott insulators and metals. In a cluster Mott insulator, Coulomb repulsion dominates over *inter*-cluster hopping, causing an insulating state, while large intra-cluster hopping t yields quasimolecular orbitals delocalized over a small cluster, e.g., a Ru dimer. The emergent internal degrees of freedom yield variable quasimolecular magnetic moments that can be tuned by electronic parameters[27,28]. In a simple cluster picture, one can distinguish the Mott limit, in which on-site Coulomb repulsion $U \gg t$ suppresses charge fluctuations between Ru sites, and the cluster Mott limit $t \gg U$. Such states may

---

[1]Institute of Physics II, University of Cologne, Cologne, Germany. [2]Department of Physics, Stockholm University, AlbaNova University Center, Stockholm, Sweden. [3]Sect. Crystallography, Institute of Geology and Mineralogy, University of Cologne, Cologne, Germany. [4]PETRA III, Deutsches Elektronen-Synchrotron DESY, Hamburg, Germany. [5]Institute for Theoretical Solid State Physics, IFW Dresden, Dresden, Germany. [6]Institute for Theoretical Physics and Würzburg-Dresden Cluster of Excellence ct.qmat, Technische Universität Dresden, Dresden, Germany. [7]Stockholm University, Stockholm, Sweden.
✉ e-mail: grueninger@ph2.uni-koeln.de

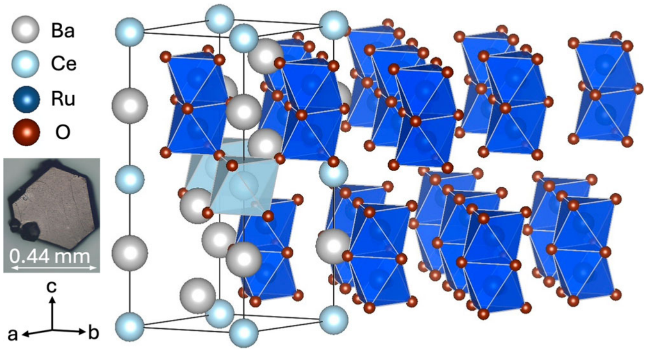

Fig. 1 | Hexagonal crystal structure of $Ba_3CeRu_2O_9$. The unit cell hosts two distinct orientations of structural dimers, each built by two face-sharing RuO_6 octahedra. The dimers grow along the *c* axis and form triangular layers. Beyond the unit cell, only the Ru_2O_9 dimers are sketched for clarity. The photo shows one of the measured crystals.

be realized in the large family of hexagonal perovskites with face-sharing RuO_6 octahedra[29]. Compounds of 6*H*-type $Ba_3MRu_2O_9$ exist for many different *M* ions[30–32], e.g., Na^+, Zn^{2+}, La^{3+}, and Ce^{4+} and host structural Ru dimers, see Fig. 1. The short intra-dimer Ru-Ru distance $d \approx 2.5$ to 2.8 Å is expected to yield large hopping[27]. Concerning magnetism, the triangular layers of dimers show geometrical frustration in the case of antiferromagnetic couplings between dimers. However, one first has to address the character of the possibly quasimolecular moments. In resonant inelastic x-ray scattering (RIXS) on the isostructural 5*d* iridates $Ba_3MIr_2O_9$ (M = Ce, Ti, In)[33–35], the quasimolecular character has been demonstrated, with the (anti-) bonding orbitals for large ζ being formed from spin-orbit entangled *j* states. The spin-liquid candidate $Ba_3InIr_2O_9$ hosts quasimolecular $j = 3/2$ moments[34] and shows persistent spin dynamics down to 20 mK[36].

The 4*d* ruthenates cover a different part of phase space, with smaller hopping, larger correlations, and smaller but still sizable spin-orbit coupling. For $Ba_3MRu_2O_9$, an exact diagonalization (ED) study finds a variety of different states with anisotropic and temperature-dependent magnetic moments that depend on electron filling, correlations, and ζ[27]. Experimentally, the reported behavior is diverse. For $M = Na^+$, charge order with a segregation into Ru^{5+} and Ru^{6+} dimers has been claimed[37], while a spin $S = 3/2$ Mott insulator has been found for $M = Zn^{2+}$ with $4d^3$ Ru^{5+} ions[38]. For $M = La^{3+}$, the results range from ferromagnetic double exchange interactions between the two Ru sites[39] via an orbital-selective $S = 3/2$ scenario[40] to a quasimolecular picture[41]. The electronic states are highly sensitive to small structural changes caused by different M^{3+} ions[39–42]. Finally, studies of polycrystalline $4d^4$ $Ba_3CeRu_2O_9$ with Ce^{4+} and Ru^{4+} ions find non-magnetic behavior that has been discussed in the Mott limit[30] and in the quasimolecular limit[43].

This diversity of partially conflicting results reflects the intertwined coupling of orbitals and spins on a dimer. Hopping *t* does not only compete with on-site *U* but also with Hund's coupling J_H and the trigonal crystal-field splitting Δ_{trig}. Furthermore, the trigonal symmetry splits the t_{2g} manifold in a_{1g} and e_g^π orbitals with different hopping strengths $t_{a_{1g}}$ and $t_{e_g^\pi}$, promoting orbital-selective behavior[2–5]. For $\zeta = 0$, this yields a multitude of possible ground states which depend on the subtle hierarchy of electronic parameters[3], and finite ζ further expands the picture[27].

Here, we address the electronic structure of the four-hole dimer compound $Ba_3CeRu_2O_9$ with RIXS at the Ru L_3 edge. We observe a rich excitation spectrum and a **q**-dependent modulation of the RIXS intensity. This allows us to determine the electronic parameters and the spin-orbit entangled singlet character of the ground state. Using exact diagonalization, we characterize the different states that emerge for either small or large hopping and different crystal-field splittings. Based on, e.g., the degree of Mott localization, we show that $Ba_3CeRu_2O_9$ is best described as being located in the intriguing intermediate regime, combining aspects of the Mott limit and of the quasimolecular limit.

RIXS interferometry is a technique very well suited for revealing a possible cluster Mott character[33–35]. In analogy to Young's double-slit experiment, the RIXS intensity of quasimolecular dimer excitations exhibits a sinusoidal interference pattern as a function of the transferred momentum **q**, arising from coherent scattering on the two dimer sites[33]. The interference pattern reveals the symmetry and character of the quasimolecular wavefunction, as demonstrated in the hard x-ray range for a series of 5*d* compounds with dimers, trimers, and tetrahedral clusters[28,34,35,44–47]. For tender x-rays at the Ru L_3 edge, one has to cope with the smaller range of **q** that can be covered. However, RIXS interferometry has even been employed in the soft X-ray range, e.g., for O_2 molecules at the O *K* edge[48] and for magnetic excitations at the Fe *L* edge[49].

Results

RIXS data

We studied Ru L_3-edge RIXS on single crystals of hexagonal $Ba_3CeRu_2O_9$, see Methods. We employed two different sample orientations, a (110) surface and a (001) surface. The resonance behavior of the RIXS intensity is presented in Fig. 2. The spectra were measured on the (001) facet for incident energies between 2.835 and 2.842 keV. The most prominent RIXS feature is observed at about 3.5 eV energy loss and corresponds to excitations from t_{2g} to e_g states. The excitation energy of 3.5 eV provides an estimate of the cubic crystal-field splitting 10 Dq. This t_{2g}-to-e_g peak is resonantly enhanced at E_{in} = 2.841 keV. In the following, we focus on the intra-t_{2g} excitations below 2 eV energy loss that resonate at a lower energy of about 2.838 keV.

RIXS spectra for the two different sample orientations are shown in Fig. 3a and b. The data cover a broad range of the angle of incidence θ with fixed modulus $|\mathbf{q}|$, and the corresponding ($h\,k\,l$) values are depicted in the insets. The spectra are very rich with prominent RIXS peaks at about 0.10, 0.26, 0.53, 0.80, 1.1, and 1.6 eV. For all of them, the RIXS intensity strongly depends on θ. As shown below, this originates from a q dependence of the intensity and from polarization effects.

In $Ba_3CeRu_2O_9$, a comprehensive description of the excitations requires to consider the interplay and competition of Coulomb interactions, hopping, crystal-field splitting, and spin-orbit coupling. This yields a large number of excitation energies, preventing a simple peak assignment. The lowest peak at 0.10 eV reflects the energy scale of spin-orbit coupling ζ but, as shown below, also is sensitive to hopping. In inelastic neutron scattering on polycrystalline samples, magnetic modes have been observed at 70 and 90 meV[43]. The peak at 0.26 eV can be traced back to hopping and ζ (see below). The peaks above 0.5 eV predominantly can be attributed to the interplay of the trigonal crystal field, Hund's coupling, and hopping.

RIXS is the ideal tool to probe the quasimolecular character of excitations, as mentioned in the introduction. With the dimer axis parallel to *c* and an intra-dimer distance *d*, the interference pattern is expected to show a period $l_0 = c/d = 5.9$ as a function of *l*. The data in Fig. 3a roughly cover the range from $l = -2.9$ to 2. In particular, the peak at 0.1 eV exhibits a pronounced, non-monotonic variation of the intensity as a function of *l*. However, we additionally have to consider polarization effects. This is illustrated in Fig. 3b, which shows spectra measured on the (001) surface. Again, strong intensity changes are observed as a function of θ. Note, e.g., the different peak intensities for the two curves measured with ($-0.7\ 0\ 4.3$) (dark red) and ($0.7\ 0\ 4.3$) (blue) with the same value of *l*. This particular intensity change cannot be caused by the dimer interference but must originate from polarization effects. In general, it is not trivial to quantitatively disentangle polarization and interference effects. Due to the many-body character of the states, the RIXS intensity is the squared sum of several terms, which leads to a full mixing of these effects. However, further insights can be obtained via a careful comparison with theory, as discussed below.

Hamiltonian

For a Ru dimer with four t_{2g} holes, we focus on the intra-t_{2g} excitations below 2 eV. On each of the two sites, i = 1 and 2, we have to consider spin-orbit coupling ζ, trigonal crystal-field splitting Δ_{trig}, and Coulomb repulsion in terms of Hubbard U and Hund's coupling J_{H}. The trigonal crystal field splits the t_{2g} manifold into a_{1g} and e_g^π orbitals. Intersite hopping is diagonal for a_{1g} and e_g^π orbitals and is parameterized by $t_{a_{1g}}$ and $f = t_{e_g^\pi}/t_{a_{1g}}$. The Hamiltonian reads[27,33,44]

$$H = \sum_i \left(H_{\mathrm{SOC},i} + H_{\Delta,i} + H_{\mathrm{C},i} \right) + H_t. \tag{1}$$

The explicit terms are given in the *Supplementary Information*. For U, J_{H}, and ζ, the relevant parameter range is well established from previous results on strongly correlated ruthenates. The on-site Coulomb repulsion U is typically found to be 2 to 2.5 eV, J_{H} is reported between 0.25 and 0.35 eV, and results for ζ range from 0.08 to 0.15 eV [13,17,18,21,41,50–52]. In contrast, the crystal-field splitting Δ_{trig} and the hopping parameters $t_{a_{1g}}$ and $t_{e_g^\pi}$ may vary strongly between different compounds.

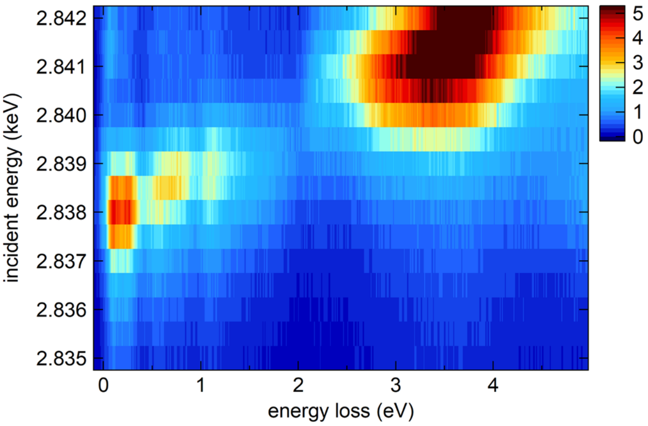

Fig. 2 | Resonance map of Ba$_3$CeRu$_2$O$_9$ at 20 K. The RIXS intensity is plotted for different incident energies across the Ru L_3 edge. The data were taken on the (001) facet. Excitations from t_{2g} to e_g states are peaking at about 3.5 eV for $E_{\mathrm{in}} \approx$ 2.841 keV, while intra-t_{2g} excitations below 2 eV energy loss are resonantly enhanced at $E_{\mathrm{in}} \approx$ 2.838 keV.

Individual 4d^4 Ru sites

We first address the electronic states of a single 4d^4 Ru site, i.e., a site with two t_{2g} holes, providing a suitable starting point for the discussion of a dimer. In cubic symmetry and for $\zeta = 0$, Coulomb interactions lift the degeneracy of the t_{2g}^4 states, giving rise to a $^3T_1$ ground state and excitations at $2J_{\mathrm{H}}$ ($^1T_1$, ^1E) and $5J_{\mathrm{H}}$ ($^1A_1$)[16]. Spin-orbit coupling splits the $^3T_1$ multiplet into a J = 0 ground state and the J = 1 and 2 excited states at $\zeta/2$ and $3\zeta/2$, see Fig. 4**a**. In the ruthenates, one finds $J_{\mathrm{H}}/\zeta \approx$ 2 to 3, such that the two types of excitations with energies $\propto \zeta$ and $\propto J_{\mathrm{H}}$ are well separated in cubic compounds such as 4d^4 K$_2$RuCl$_6$[13]. The equivalent intra-t_{2g} excitations also have been observed in, e.g., RIXS on cubic 5d^4 K$_2$OsCl$_6$[53]. The RIXS intensity of excitations from $J = 0$ to the $^1A_1$ multiplet at $5J_{\mathrm{H}}$ vanishes for a scattering angle of 90°[53], as used in our experiment.

In the ruthenates, the non-cubic crystal field splitting often is larger than ζ. A large crystal field splits the multiplets at $2J_{\mathrm{H}}$ as well as the ninefold degenerate $^3T_1$ multiplet. Combined with spin-orbit coupling, this gives rise

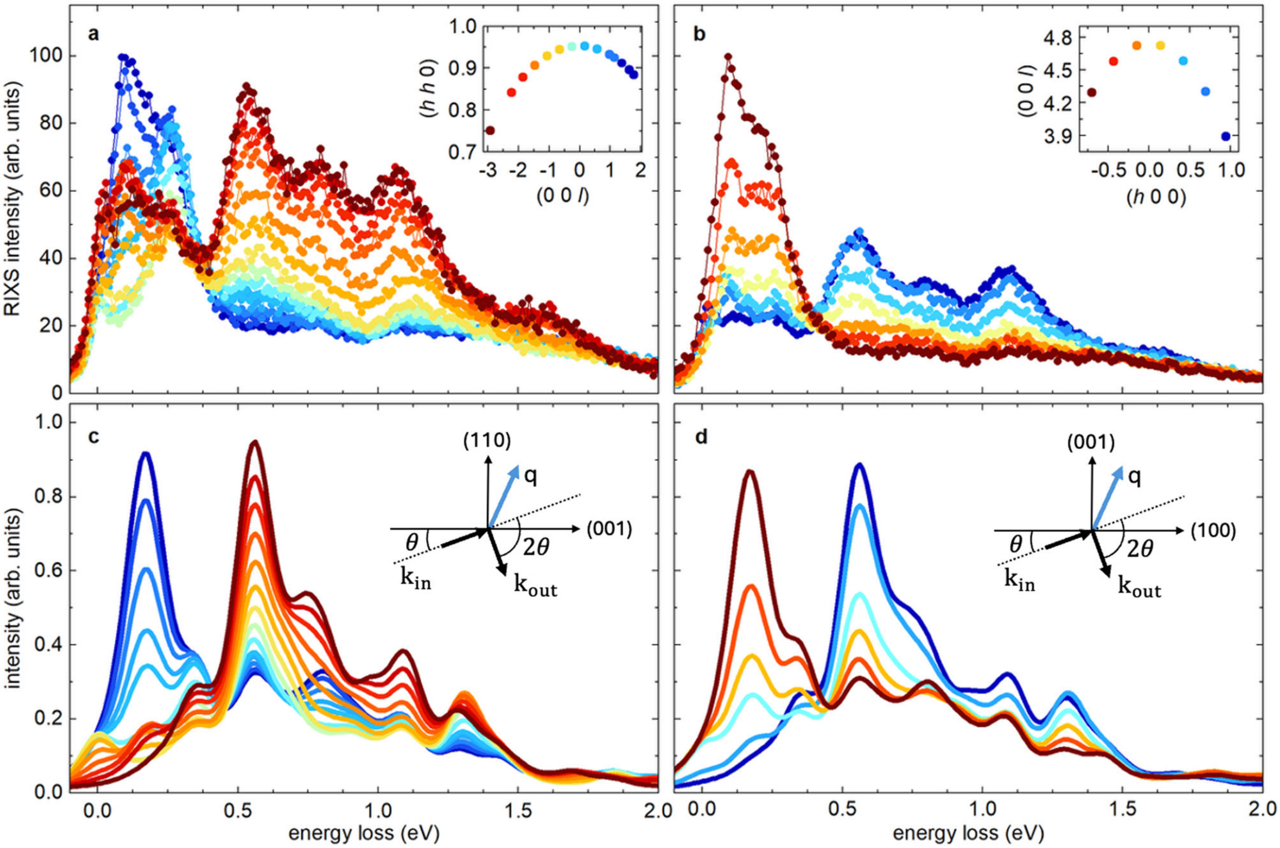

Fig. 3 | RIXS spectra of Ba$_3$CeRu$_2$O$_9$. Data have been measured at 20 K on **a** the (110) surface and **b** the (001) surface for different angles of incidence θ with fixed modulus |**q**|, i.e., fixed scattering angle 2θ = 90°, see sketches in **c** and **d**. The corresponding (h k l) values are given in the insets. **c**, **d**: Calculated spectra for the orientations used in **a**, **b**. We employed U = 2 eV, J_{H} = 0.26 eV, ζ = 0.15 eV, Δ_{trig} = 0.27 eV, $t_{a_{1g}}$ = 0.66 eV, and $f = -0.45$ (i.e., $t_{e_g^\pi} = -0.30$ eV). For plotting, we further assumed a peak width of 90 meV.

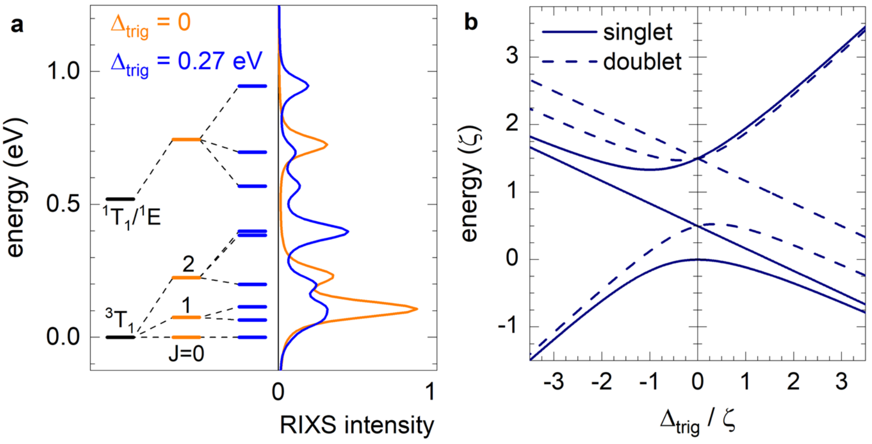

Fig. 4 | Response of a single t_{2g}^4 site. a The left panel shows the cubic multiplets (black) and how they are split by spin-orbit coupling (orange) and a trigonal crystal field (blue). The right panel depicts the corresponding calculated RIXS spectra for $\zeta = 0.15$ eV, $J_H = 0.26$ eV, and $\Delta_{trig} = 0$ or 0.27 eV. **b** Energies within the $^3T_1$ manifold as a function of Δ_{trig}/ζ in the limit of large J_H. For $\Delta_{trig} = 0$, the states at 0, $\zeta/2$, and $3\zeta/2$ correspond to $J = 0$, 1, and 2, respectively.

to a rich behavior at low energies, see Fig. 4. With RIXS, the corresponding excitations have been studied in $4d^4$ Ca_2RuO_4, showing four peaks at about 0.05, 0.32, 0.75, and 1.0 eV[17]. Roughly, the lower two can be assigned to spin-orbit coupling and crystal-field splitting, while the two peaks at 0.75 and 1.0 eV correspond to the feature at $2J_H$ split by the crystal field, cf. Fig. 4. A similar case has been reported in RIXS on $4d^4$ $In_2Ru_2O_7$ at 300 K, showing five peaks at about 0.05, 0.28, 0.39, 0.70, and 1.0 eV[52].

Excitations on a dimer

In order to determine the electronic parameters, in particular $t_{a_{1g}}$, $t_{e_g^\pi}$, and Δ_{trig}, we numerically simulated the RIXS spectra, including the pronounced dependence on the scattering geometry, i.e., the sample orientation and angle of incidence θ. The latter determines both $\mathbf{q}$ and the polarization. We used least square error fitting to determine the relevant parameter regime, and then further optimized parameters in a narrow range. The calculated spectra reproduce the key characteristics of the experimental data, see Fig. 3. The simulations describe the overall peak structure with two dominant peaks below 0.4 eV and four main RIXS features above 0.5 eV. The main shortcoming is that the energies of the two lowest peaks are slightly too high in the calculations. However, the chosen parameter set considers the peak energies, the overall line shape, and the θ dependence of the intensity. We in particular achieve a good description of the latter, showing opposite behavior at low and high energies and for the two sample orientations. On the (110) surface, Fig. 3**a**, the intensity is maximized for small θ (blue curve; positive l) below about 0.4 eV but for large θ (dark red; negative l) at higher energies, giving rise to a kind of isosbestic point at 0.4 eV where the RIXS intensity is nearly independent of θ. The data on the (001) surface show the opposite behavior, with the intensity at low energy being maximized for large θ (dark red curve; negative h). These features are very well reproduced by the simulation.

Optimal agreement between theory and experiment is obtained for $U = 2$ eV, $J_H = 0.26$ eV, and $\zeta = 0.15$ eV. These values are within the range established by previous studies on $4d$ ruthenates[13,17,18,21,41,50–52]. For the more material-specific parameters we find $\Delta_{trig} = 0.27$ eV, $t_{a_{1g}} = 0.66$ eV, and $f = -0.45$. A value of f close to $-1/2$ agrees with theoretical predictions for face-sharing octahedra[27]. Large hopping $t_{a_{1g}} \gtrsim 0.7$ eV has also been reported for $Ba_3LaRu_2O_9$ with five t_{2g} holes per dimer[41]. Density-functional theory predicts $t_{a_{1g}} \approx 0.4-0.8$ eV for face-sharing ruthenates[27]. In $Ba_3CeRu_2O_9$, the octahedra are elongated along the dimer axis, indicating a negative point-charge contribution to Δ_{trig} in the hole picture, but a dominant covalent contribution may reverse the sign[54,55].

For the peak assignment, Fig. 5 shows the excitation energies for the best parameter set. In the left panel, we start with $U = 2$ eV and switch on J_H up to 0.26 eV. The two red lines denote the excitations of a single site at $2J_H$ and $5J_H$. Three further lines correspond to excitations on both sites with total excitation energies of $4J_H$, $7J_H$, and $10J_H$. For vanishing hopping, such double excitations have zero intensity in RIXS. The latter is also valid for the excitation at $U - 3J_H$, i.e., with an energy that *decreases* with increasing J_H. It corresponds to the lowest intersite excitation, $d_1^4 d_2^4 \rightarrow d_1^3 d_2^5$[16]. The second panel depicts the effect of varying Δ_{trig} from 0 to 0.27 eV. The red lines again refer to a single site, showing the splitting of the cubic multiplets, see also Fig. 4. Finally, the third and fourth panels show the effects of hopping and spin-orbit coupling, respectively. The underlying color plot depicts the calculated RIXS intensity for $l = -2$. In contrast, the fifth panel employs $l = 2$, highlighting the low-energy peaks, cf. Fig. 3**c**.

Intra-dimer hopping substantially increases the number of distinct excitation energies. Remarkably, most excitation energies increase with increasing hopping, showing that the ground-state energy E_0 is one of those that benefit the most. Concerning the ground state, we find a level crossing at $t_{a_{1g}} \approx 0.4$ eV, which is evident from a jump in the RIXS intensity, see Fig. 5. The character of the ground state will be discussed below. Here we only mention that, for small $t_{a_{1g}}$, the energy is lowered $\propto t_{a_{1g}}^2/U$, as expected for a Mott insulator with exchange interactions. This picture breaks down due to level crossing. However, even for $t_{a_{1g}}$ around 0.66 eV we find that E_0 is lowered roughly quadratically in hopping. The behavior strongly differs from the energy of a bonding state that decreases linearly in hopping in the fully delocalized quasimolecular limit. This reflects the rather localized character of the states, despite the large hopping and the breakdown of the exchange limit.

Based on the more localized character, the results for a single site discussed above to some extent provide a guideline for the interpretation of some of the RIXS peaks of $Ba_3CeRu_2O_9$. This works in particular at high energy and as long as the hopping-induced energy shifts are small compared to $2J_H$, which is true for many but not all of the states. The RIXS peaks at 0.8 and 1.1 eV are related to the multiplets at $2J_H$, split by Δ_{trig} and shifted in energy by hopping, see Fig. 5. The peak at 0.53 eV predominantly can be traced back to the effect of Δ_{trig} and hopping. Remarkably, the three energies of 0.53, 0.80, and 1.1 eV are roughly 0.1 eV higher than the peak energies reported for single-site $4d^4$ Ca_2RuO_4 and $In_2Ru_2O_7$[17,52]. This may indicate a common origin, where the energy shift in $Ba_3CeRu_2O_9$ is caused by the hopping-induced lowering of the ground state.

The low-energy peak at 0.1 eV can be attributed to spin-orbit coupling, see Fig. 5, which again to some extent is reminiscent of Ca_2RuO_4 and $In_2Ru_2O_7$[17,52]. In $Ba_3CeRu_2O_9$, however, one has to address the effect of spin-orbit coupling on the low-energy dimer states, for which hopping is essential, as discussed below. Finally, excitations around 0.26 eV mainly arise due to hopping, but also spin-orbit coupling plays a role, see Fig. 5.

Intensity modulation

The excellent description of the θ dependence of the RIXS intensity is a strong asset of our theoretical result. The angle of incidence θ sets polarization and $\mathbf{q}$, and both affect the intensity. For RIXS on a dimer with quasimolecular states, a given excited state can be reached by scattering on either of the two sites. Summation over the coherent scattering processes

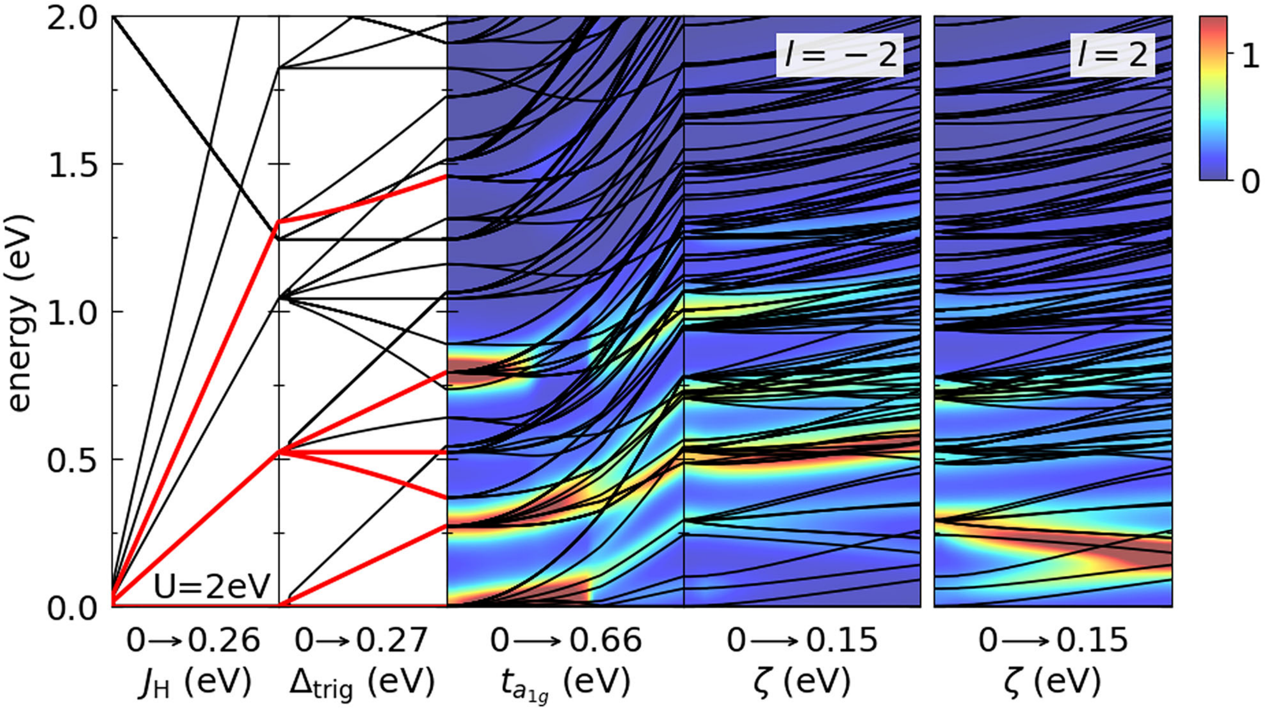

Fig. 5 | Excitation energies and RIXS intensity of a face-sharing dimer with four t_{2g} holes. From left to right, different parameters are successively included. We use $U = 2$ eV and first increase J_H from 0 to 0.26 eV, then Δ_{trig} from 0 to 0.27 eV, hopping $t_{a_{1g}}$ up to 0.66 eV with fixed $f = -0.45$, and finally ζ from 0 to 0.15 eV. The red lines in the first two panels represent the energies of a single site with two holes. The color plot in the third and fourth panels shows the calculated RIXS intensity for the (110) orientation with $2\theta = 90^\circ$ and $l = -2$ for a peak width of 50 meV. The last panel again depicts the energies as a function of ζ but employs $l = 2$ for the RIXS intensity to highlight the behavior at low energies, cf. Fig. 3c.

yields a sinusoidal intensity modulation[33]. With inversion symmetry, one expects either $\sin^2(\pi l/l_0)$ or $\cos^2(\pi l/l_0)$ behavior (with $l_0 = c/d$), depending on the parity of the involved states. The excitation from an, e.g., even ground state to an even excited state with identical matrix elements on both sites yields a $\cos^2(\pi l/l_0)$ modulation. A face-sharing dimer does not obey inversion symmetry, but the crystal structure shows two dimer orientations that are rotated by π around c, see Fig. 1. Summing over both orientations again yields a $\sin^2(\pi l/l_0)$ or $\cos^2(\pi l/l_0)$ interference pattern[33].

In a Mott insulator, the picture is different. For a strictly local excitation on site i, the RIXS intensity does not depend on $\mathbf{q}$[35]. Orbital excitations typically are considered to be such local excitations, e.g., from $|xy\rangle_i$ to $|yz\rangle_i$. In this example, exchange coupling between the two dimer sites will yield states $|yz\rangle_1 \pm |yz\rangle_2$ but this will only cause a modulation if the energy separation is larger than the peak width. Note that a large energy splitting marks the crossover to the quasimolecular cluster Mott case. In the Mott limit, the superposition of overlapping $\sin^2(\pi l/l_0)$ and $\cos^2(\pi l/l_0)$ modulations gives constant intensity as a function of $\mathbf{q}$. The situation is different for excitations between entangled states, which in the Mott limit typically is the case for spin excitations. For simplicity, we consider two sites carrying $S = 1/2$ each. The excitation from a singlet $(|\uparrow\downarrow\rangle - |\downarrow\uparrow\rangle)/\sqrt{2}$ to a triplet state $|\uparrow\uparrow\rangle$ can be reached by a spin flip on either of the two sites. This again yields a sinusoidal intensity modulation, as observed for the bond-directional magnetic excitations in the Kitaev material $\mathrm{Na_2IrO_3}$[56,57].

In both the Mott limit and the cluster Mott limit, a possible modulation will show minimum or maximum intensity for $l = 0$, which is covered by the (110) orientation. The experimental data indeed show minimum intensity close to $l = 0$ below 0.35 eV as well as around 1.7 eV. This is highlighted in Fig. 6, which shows the RIXS intensity integrated over selected energy ranges, both for experiment and theory. Below 0.35 eV (blue and green) and above 1.55 eV (black), the integrated intensity clearly shows non-monotonic behavior, and the modulation agrees with a $\sin^2(\pi l/l_0)$ behavior that acquires asymmetry with respect to $l = 0$ due to polarization effects.

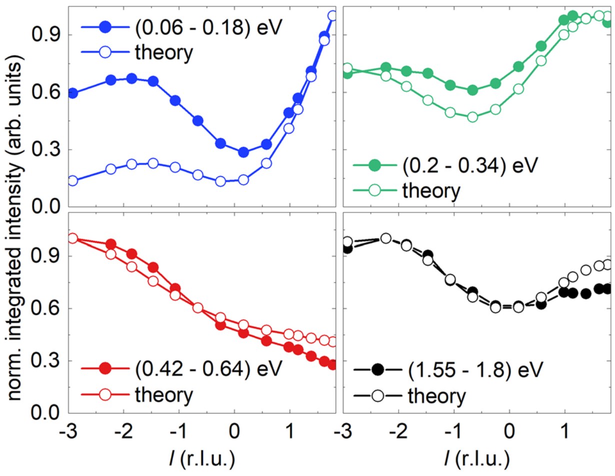

Fig. 6 | RIXS intensity as a function of *l*. The experimental data (full symbols) have been integrated over the indicated energy intervals and normalized to the maximum value. The corresponding simulations have been evaluated over the respective peak regions. The calculations reproduce the overall behavior of the experimental result very well.

In contrast, we find a monotonic decrease of intensity around, e.g., 0.5 eV, which we attribute to dominant polarization effects. These arise because a change of $\mathbf{q}$ is accompanied by a change of the actual scattering geometry, i.e., θ. This assignment is supported by simulations for a single $4d^4$ site with identical parameters, in particular positive Δ_{trig} but vanishing hopping. We find a very similar monotonic trend for the θ dependence with opposite behavior at low and high energies and for the two sample orientations, see *Supplementary Information*.

In the $5d$ iridate dimers $\mathrm{Ba_3}M\mathrm{Ir_2O_9}$, the entire intra-$t_{2g}$ excitation spectrum shows strong modulation of the RIXS intensity[33–35]. The ruthenate

$Ba_3CeRu_2O_9$ shows a different behavior. The modulation for many peaks is suppressed or overruled by polarization effects, pointing to a more local character. However, this may also be caused by averaging over the large number of excitations of the four-hole dimer, see Fig. 5. Finally, the observation of a pronounced modulation as a function of l both at low and high energies supports a partially quasimolecular character. Overall, the intensity modulation supports the picture of $Ba_3CeRu_2O_9$ being located in the intermediate regime. However, to quantitatively understand the puzzling character of the ground state, we have to address the wavefunction obtained in our simulations of the RIXS data.

Character of electronic states

For the four-hole Ru dimers, the competition of Coulomb repulsion, hopping, crystal-field splitting, and spin-orbit coupling allows for several distinct ground states. In the following, we discuss their character and compare in particular the local Mott limit and the quasimolecular limit before addressing the crossover regime. We substantiate the claim that $Ba_3CeRu_2O_9$ is best described as being in the intermediate regime.

Mott limit for $\zeta = 0$. We start from $\zeta = 0$, a case that is often addressed for ruthenates and other $4d$ compounds[4], also in previous reports on $Ba_3CeRu_2O_9$[30,43]. Indeed we find that the results for $\zeta = 0$ are helpful for understanding the physics for finite ζ. In the localized Mott limit, Coulomb repulsion suppresses charge fluctuations such that each Ru site hosts two t_{2g} holes. Hund's coupling then favors local $S = 1$ configurations. The resulting dimer ground state depends sensitively on the trigonal crystal-field splitting Δ_{trig}, which controls the orbital occupancy, and on the strength of hopping. The corresponding phase diagram is summarized in Fig. 7a for $U = 2$ eV, $J_H = 0.26$ eV, and $f = -0.45$.

For $t_{a_{1g}} = 0$, each Ru site shows 3-fold spin degeneracy. The orbital degeneracy depends on Δ_{trig}, which yields dimer ground states with total degeneracy of either 36, 81, or 9 for Δ_{trig} being positive, zero, or negative, respectively. Small hopping $t_{a_{1g}}$ causes exchange interactions between the $S = 1$ sites. Both antiferromagnetic and ferromagnetic coupling can be realized, yielding $S_{\mathrm{tot}} = 0$ in states I and III but $S_{\mathrm{tot}} = 2$ in state II. The corresponding sketches in Fig. 7c illustrate this exchange-dominated case of small hopping. In I for $\Delta_{\mathrm{trig}} > 0$, one hole per site occupies the a_{1g} orbital and the second one an e_g^π orbital. In this situation, hopping $t_{e_g^\pi}$ between the degenerate e_g^π orbitals yields a Kugel-Khomskii-type exchange that favors parallel spin alignment and the occupation of different orbitals. However, this is overruled by the stronger $t_{a_{1g}}$ that favors antiparallel spin alignment. Altogether, only a two-fold orbital degeneracy remains in state I with $S_{\mathrm{tot}} = 0$. In state III for $\Delta_{\mathrm{trig}} < 0$, both holes preferentially occupy the e_g^π sector, so that the orbital degeneracy is removed already at the local level, see Fig. 7c. In the weak-hopping limit, antiferromagnetic exchange yields $S_{\mathrm{tot}} = 0$ for III. Note that state III is continuously connected to the quasimolecular limit discussed below.

In contrast, state II is realized for small Δ_{trig} with nearly degenerate orbitals. In this case, the larger a_{1g} hopping selects configurations with in total one a_{1g} hole, while Hund's coupling favors parallel spins in the virtual intermediate states. As a result, the effective interaction between the two sites is ferromagnetic and the dimer realizes a high-spin state with $S_{\mathrm{tot}} = 2$. This may be viewed as a form of double exchange[3,4], in which the strongly hopping a_{1g} hole mediates ferromagnetic coupling between the more localized e_g^π degrees of freedom. Because the e_g^π orbitals remain degenerate, state II carries a 2-fold orbital degeneracy on top of the 5-fold spin degeneracy.

Quasimolecular limit for $\zeta = 0$. In the opposite limit of dominant intra-dimer hopping, the most appropriate description is in terms of bonding and antibonding quasimolecular orbitals. Because $|t_{a_{1g}}| > |t_{e_g^\pi}|$, the bonding a_{1g} orbital is filled first, while the remaining two holes occupy the bonding e_g^π sector. Hund's coupling then favors a triplet with $S_{\mathrm{tot}} = 1$, see state IV in Fig. 7c. For $\Delta_{\mathrm{trig}} > 0$, this regime with $S_{\mathrm{tot}} = 1$ is reached already for moderate hopping $t_{a_{1g}}$ ≈0.4 eV (see Fig. 7a), where the ground state exhibits substantial localized character. However, it is continuously connected to the quasimolecular limit, see next paragraph and Fig. 8. Phase IV extends to increasingly negative values of Δ_{trig} as the hopping increases. This can be understood naturally from the quasimolecular perspective: because $|t_{a_{1g}}| > |t_{e_g^\pi}|$, the energy gain associated with occupying the bonding a_{1g} orbital eventually outweighs the crystal-field energy cost incurred for $\Delta_{\mathrm{trig}} < 0$. However, for a given value of hopping, large negative Δ_{trig} causes a transfer of holes from bonding a_{1g} to bonding e_g^π, leaving either one or zero a_{1g} holes in states V and III, respectively.

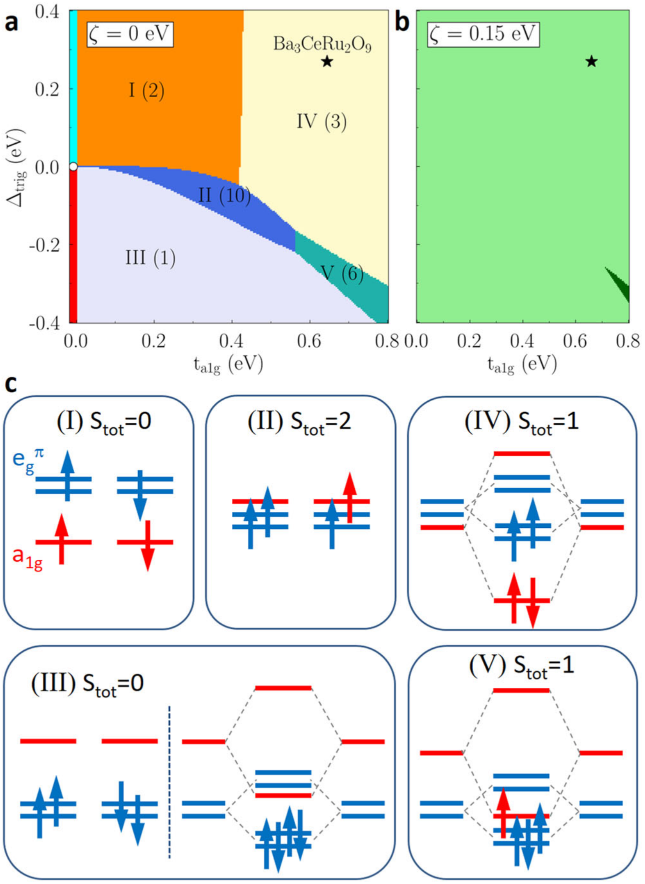

Fig. 7 | Ground states of a four-hole dimer in different limits. **a** For $\zeta = 0$, we find several ground states as a function of Δ_{trig} and $t_{a_{1g}}$. The dominant states I-V for $t_{a_{1g}} > 0$ are plotted for $U = 2$ eV, $J_H = 0.26$ eV, and $t_{e_g^\pi}/t_{a_{1g}} = -0.45$. The numbers in parentheses give the degeneracy. Note that there are several tiny pockets of further phases at some parts of the phase boundaries that are not resolved in the figure and are irrelevant for our discussion. Additionally, the three states for $t_{a_{1g}} = 0$ and positive, vanishing, or negative Δ_{trig} are indicated on the very left. **b** Phase diagram for $\zeta = 0.15$ eV. A spin-orbital singlet state (light green) dominates, and the parameter region with orbital degeneracy (dark green) has shrunken considerably. **c** The sketches illustrate the limiting cases of either very small or very large hopping. For state III, these two limits are continuously connected. For state IV, the continuous change from the intermediate regime to the quasimolecular limit is shown in Fig. 8. The sketches depict local a_{1g} (red) and e_g^π (blue) orbitals for I-III and (anti-) bonding orbitals for III-V.

Crossover regime. Above we have identified the main character of the RIXS peaks and revealed and described the $\mathbf{q}$-dependent modulation of the RIXS intensity. Our ED simulations reproduce the main experimental RIXS features very well and constrain the relevant parameter regime. Neglecting small ζ, $Ba_3CeRu_2O_9$ lies well within the range of state IV, see star in Fig. 7a. Qualitatively, state IV is well understood in the quasimolecular limit but cannot be rationalized in the weak-coupling limit. Compared to state I, it requires a hopping of sufficient size to violate Hund's rule and obtain $S_{\mathrm{tot}} = 1$. Below we show that state IV covers both the quasimolecular limit and the intermediate regime.

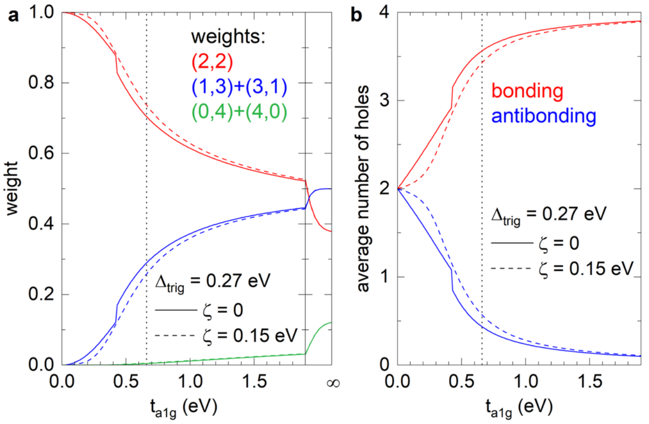

Fig. 8 | Contributions to the ground state wave function. a Cumulated weights w_{nm} for n holes on one site. For $t_{a_{1g}} = \infty$, we find $w_{22} = 3/8$, $w_{13} + w_{31} = 1/2$, and $w_{04} + w_{40} = 1/8$. **b** Average number of holes in (anti-) bonding orbitals. In **a** and **b**, the data are plotted along a cut through Fig. 7a for $\Delta_{\mathrm{trig}} = 0.27$ eV with otherwise identical parameters. The jump at $t_{a_{1g}} \approx 0.4$ eV for $\zeta = 0$ marks the phase transition between states I and IV. The vertical dotted line denotes $t_{a_{1g}} = 0.66$ eV as appropriate for $Ba_3CeRu_2O_9$.

To address the crossover regime quantitatively, Fig. 8a shows the cumulated weights w_{nm} of terms in the ground state that host n holes on one site and $m = 4 - n$ on the other. The weights are plotted as a function of $t_{a_{1g}}$ along a cut through Fig. 7a for $\Delta_{\mathrm{trig}} = 0.27$ eV. For small hopping, the Mott limit shows two holes on each site, $w_{22} \approx 1$, minimizing Coulomb energy. With increasing hopping, kinetic energy overrules Coulomb repulsion. This yields an increase of the weight of states with three or four holes on one of the sites. In the limit of $t_{a_{1g}} = \infty$, we find $w_{22} = 3/8$ while 50 % of the weight is carried by states with three holes on one site. Accordingly, w_{22} provides a quantitative measure of the degree of Mott localization. Note the jump of w_{22} at the phase transition around $t_{a_{1g}} = 0.4$ eV, indicating the more localized character of state I compared to state IV, see Fig. 7. The phase transition and the jump are washed out by spin-orbit coupling $\zeta = 0.15$ eV. For $Ba_3CeRu_2O_9$ with $t_{a_{1g}} = 0.66$ eV, we find $w_{22} = 0.70$ for $\zeta = 0$ and 0.74 for $\zeta = 0.15$ eV, which is in the intermediate regime but still closer to the Mott limit than to the quasimolecular limit.

Alternatively, we consider a quasimolecular basis with (anti-) bonding orbitals. Figure 8b depicts the average number of holes in bonding or antibonding states, n_{B} and n_{AB}, respectively. In the quasimolecular limit, all four holes occupy bonding orbitals, $n_{\mathrm{B}} \approx 4$. In the Mott limit, the occupation probability of bonding and antibonding orbitals is equal, $n_{\mathrm{B}} = n_{\mathrm{AB}} = 2$. Like w_{22}, also n_{B} jumps at the phase transition at $t_{a_{1g}} \approx 0.4$ eV, reflecting the more delocalized character of state IV. The jump occurs around $n_{\mathrm{B}} = 3$, halfway between the Mott limit and the quasimolecular limit. For $t_{a_{1g}} = 0.66$ eV (vertical dotted line), we find $n_{\mathrm{B}} = 3.6$ for $\zeta = 0$ and 3.4 for $\zeta = 0.15$ eV. This is an interesting result: Using a quasimolecular basis, the average number of holes in bonding orbitals tends to the side of the quasimolecular limit. At the same time, a description in terms of localized states shows that the contribution of Mott-like terms with two holes per site is closer to the Mott limit. This demonstrates the intermediate character of $Ba_3CeRu_2O_9$ in a quantitative way. It moreover shows that a comparison of the two approaches is important to obtain a comprehensive picture.

Nature of the ground state for finite ζ

The phase diagram for finite ζ looks much simpler, see Fig. 7b. However, finite ζ does not qualitatively invalidate our classification for $\zeta = 0$. Spin-orbit coupling removes some of the exact degeneracies and turns the level crossings of the $\zeta = 0$ phase diagram into avoided crossings. The main character of the ground state nevertheless changes as a function of hopping and Δ_{trig}, and the analysis for $\zeta = 0$ provides a useful guide. In particular, it remains valid that $Ba_3CeRu_2O_9$ lies outside the weak-coupling regime of simple exchange between localized states. To gain further insight, we approximate the ED ground state by simple trial wave functions.

Mott limit for finite ζ. About 74 % of the ground-state weight resides in configurations with two holes on each Ru site. This is within the crossover regime but still closer to the value for $t_{a_{1g}} = 0$ (100 %) than for $t_{a_{1g}} = \infty$ (37.5 %), motivating a description in terms of local building blocks. Finite ζ lifts the degeneracy within the e_g^π sector. Using the complex orbitals $e_{g\pm}^\pi$ is the most convenient choice, as ζ merely shifts $|e_{g+}^\pi, \uparrow\rangle$ and $|e_{g-}^\pi, \downarrow\rangle$ upwards in energy without mixing with the a_{1g} orbitals. In good approximation, we may restrict the discussion to

$$|a_{1g}, \sigma\rangle \equiv |a\sigma\rangle, \quad |e_{g+}^\pi, \downarrow\rangle \equiv |+\downarrow\rangle, \quad |e_{g-}^\pi, \uparrow\rangle \equiv |-\uparrow\rangle.$$

The definitions of the orbitals and their relation to the spin-orbit eigenstates $|j, j_z\rangle$ are given in the *Supplementary Information*. Using this local basis, we define the singlet states

$$\begin{aligned} |\psi_1\rangle &= \Big[|a\uparrow\rangle_1|+\downarrow\rangle_1|a\downarrow\rangle_2|-\uparrow\rangle_2 + (1 \leftrightarrow 2)\Big]/\sqrt{2} \\ |\psi_2\rangle &= \Big[|a\uparrow\rangle_1|-\uparrow\rangle_1|a\downarrow\rangle_2|+\downarrow\rangle_2 + (1 \leftrightarrow 2)\Big]/\sqrt{2} \\ |\psi_3\rangle &= \Big[|a\uparrow\rangle_1|a\downarrow\rangle_1|-\uparrow\rangle_1|+\downarrow\rangle_2 + |a\uparrow\rangle_1|a\downarrow\rangle_1|-\uparrow\rangle_2|+\downarrow\rangle_1 \\ &\quad -|a\uparrow\rangle_2|a\downarrow\rangle_1|-\uparrow\rangle_1|+\downarrow\rangle_1 \\ &\quad +(1 \leftrightarrow 2)]/\sqrt{8}\,. \end{aligned} \tag{2}$$

With the constraint $|\alpha|^2 + |\beta|^2 + |\gamma|^2 = 1$, the trial state

$$|\psi\rangle = \alpha|\psi_1\rangle + \beta|\psi_2\rangle + \gamma|\psi_3\rangle \tag{3}$$

captures more than 86 % of the ED ground state using only two independent parameters. Here, $|\psi_1\rangle$ provides the dominant contribution within the sector with two holes per site (≈ 46 %). Note that $|\psi_1\rangle$ violates Hund's rule, showing that it lies outside the weak-coupling exchange limit given by states I-III. In contrast, the smaller contribution $|\psi_2\rangle$ is connected to state I. The leading correction with asymmetric charge distribution is given by $|\psi_3\rangle$ carrying 24 % of the ED ground state.

Quasimolecular limit for finite ζ. In agreement with the intermediate nature of $Ba_3CeRu_2O_9$, the ground state can similarly be approximated in a cluster Mott picture. Remarkably, a trial state based on the quasimolecular limit performs even slightly better than the Mott limit one in Eq. (3). The simple product state

$$|\widetilde{\psi}_0\rangle = |a\uparrow\rangle_B\,|a\downarrow\rangle_B\,|-\uparrow\rangle_B\,|+\downarrow\rangle_B, \tag{4}$$

where $|\alpha\rangle_B$ denotes the bonding state of state $|\alpha\rangle$, already captures 71 % of the ED ground state.

The quasimolecular ansatz can be systematically improved by incorporating the effect of Coulomb repulsion, which enhances the weight of configurations with two holes per site and suppresses sectors with three or four holes on one site. Within the (anti-)bonding basis, this can, e.g., be achieved by admixing states with an even number of antibonding (AB) orbitals. Using

$$\begin{aligned} |\widetilde{\psi}_2\rangle &= \tfrac{1}{\sqrt{6}}\Big[|a\uparrow\rangle_{AB}\,|a\downarrow\rangle_{AB}\,|-\uparrow\rangle_B\,|+\downarrow\rangle_B \\ &\qquad +|a\uparrow\rangle_{AB}\,|-\uparrow\rangle_{AB}\,|a\downarrow\rangle_B\,|+\downarrow\rangle_B + \ldots\Big], \qquad (5) \\ |\widetilde{\psi}_4\rangle &= |a\uparrow\rangle_{AB}\,|a\downarrow\rangle_{AB}\,|-\uparrow\rangle_{AB}\,|+\downarrow\rangle_{AB}\,, \end{aligned}$$

the trial state

$$\left|\widetilde{\psi}\right\rangle = \alpha\left|\widetilde{\psi}_0\right\rangle + \beta\left|\widetilde{\psi}_2\right\rangle + \gamma\left|\widetilde{\psi}_4\right\rangle \tag{6}$$

captures 87 % of the ED ground state, again with only two independent parameters. Remarkably, we find a nearly as good description of the ED ground state by replacing the bonding and antibonding combinations of $\left\{\left|a\uparrow\right\rangle, \left|a\downarrow\right\rangle, \left|-\uparrow\right\rangle, \left|+\downarrow\right\rangle\right\}$ by those constructed from the j eigenstates $\{\left|\frac{1}{2},\frac{1}{2}\right\rangle, \left|\frac{1}{2},-\frac{1}{2}\right\rangle, \left|\frac{3}{2},\frac{1}{2}\right\rangle, \left|\frac{3}{2},-\frac{1}{2}\right\rangle\}$, see *Supplementary Information*. In face-sharing iridate dimers and trimers with large spin-orbit coupling $\zeta \approx 0.4$ eV, the quasimolecular j states provide the most appropriate basis[33,34,44]. It is astounding how well the quasimolecular j basis works even in $Ba_3CeRu_2O_9$, despite the much smaller value of ζ.

Overall, both the localized and quasimolecular constructions capture substantial fractions of the ground state. This again shows that $Ba_3CeRu_2O_9$ lies in the crossover regime between localized and quasimolecular behavior.

Discussion

The seemingly harmless non-magnetic dimer ground state of $Ba_3CeRu_2O_9$ with four holes per dimer turns out to be not trivial. It is located in the intriguing crossover regime between the local Mott limit and the quasimolecular cluster Mott limit. Using a basis of Mott localized states, the charge distribution predominantly follows the expectations for strong Coulomb repulsion favoring two holes per site. At the same time, a basis of (anti-) bonding orbitals provides a different perspective, with most of the holes occupying bonding orbitals as expected in the quasimolecular limit. Hopping is so large that the ground state cannot be described in the weak-coupling limit with exchange interactions, but it can be motivated from a quasimolecular perspective. Moreover, a simple quasimolecular trial wave function describes the ground state very well, but this also applies to a simple trial wave function based on localized states. Our results reveal the limits of the often considered dichotomy between localized states and quasimolecular states and highlight the more subtle physics of the crossover regime.

In cluster Mott insulators, the character of the quasimolecular magnetic moments is sensitive to electronic parameters[28]. For instance the $5d$ iridate $Ba_3InIr_2O_9$ with three holes per dimer is close to the transition between $j = 3/2$ and $1/2$, governed by the size of hopping[27,34]. In comparison, the crossover regime realized in the ruthenate $Ba_3CeRu_2O_9$ offers a larger variety of competing ground states as a function of hopping and trigonal crystal field, which are the electronic parameters that can be tuned most directly via, e.g., chemical pressure or external pressure. It is promising to extend our analysis to Ru dimer compounds with an odd number of holes that carry a local magnetic moment[27]. In some cases, the classification as Mott insulators vs. quasimolecular compounds may have to be revisited. Indeed, a strong sensitivity to small changes of the crystal structure has been reported for $Ba_3MRu_2O_9$ with M^{3+} ions[41]. A comprehensive picture has to include Ru dimers with an even hole count different from four. With six t_{2g} holes, $4d^3$ $Ba_3ZnRu_2O_9$ has been discussed as a $S = 3/2$ Mott insulator[38]. The half-filled t_{2g} shell is energetically favorable and may stabilize the Mott phase. In terms of local multiplets, the lowest inter-site excitation energy is as large as $U + 2J_H$ for the excitation $d_i^3 d_j^3 \rightarrow d_i^2 d_j^4$ but equals only $U - 3J_H$ for $d_i^4 d_j^4 \rightarrow d_i^3 d_j^5$[16]. However, the effect of spin-orbit coupling, pushing the four-hole dimer $Ba_3CeRu_2O_9$ to the Mott side, is strongly suppressed for a d^3 configuration[58]. It is an interesting task to quantitatively determine the role of charge fluctuations as a function of the hole count.

Spin-orbit coupling is the smallest of the electronic parameters and has often been neglected in $4d$ ruthenates. We find that comparing $\zeta = 0$ and finite ζ is most helpful for understanding the rich many-body behavior. Finite $\zeta = 0.15$ eV is decisive for the non-magnetic singlet ground state, which the four-hole dimer features in an overwhelming part of the phase diagram. This bears some analogy with the local $J = 0$ ground state of a single d^4 site that is realized irrespective of the value of $\Delta_{\mathrm{trig}}/\zeta$. For a lattice of d^4 sites with large Δ_{trig}, however, the local $J = 0$ state does not necessarily provide the most intuitive picture compared to, e.g., an effective low-energy $S = 1$ model. Similarly, the picture of a non-magnetic dimer misses the underlying sensitivity of the electronic structure to the tight competition of several electronic parameters, giving rise to a multitude of possible ground states in a $\zeta = 0$ approach and to many low-energy states.

Methods

Crystal growth and crystal structure

We studied single crystals of $Ba_3CeRu_2O_9$. Initially, polycrystalline $Ba_3CeRu_2O_9$ has been synthesized via conventional solid-state reactions, similar to previous reports[30]. The starting materials $BaCO_3$, CeO_2, and RuO_2 were weighed in appropriate metal ratios, thoroughly mixed and heated in alumina crucibles at 1573 K for 48 hours. Phase purity was examined by powder X-ray diffraction, which beyond $Ba_3CeRu_2O_9$ revealed minor secondary phases of $Ba_4CeRu_3O_{12}$ and $BaCeO_3$. Single crystals were subsequently grown using a flux method inspired by refs. 33–35,59. The prereacted polycrystalline powder was mixed with $BaCl_2 \cdot 2H_2O$ in a 1:30 molar ratio and heated in alumina crucibles to 1573 K. The melt was slowly cooled to 1173 K at a rate of 2 K/h. After cooling, residual $BaCl_2$ flux was dissolved using distilled water. For the resulting crystals, good agreement with the nominal stoichiometry was verified by energy-dispersive X-ray spectroscopy.

At 300 K, $Ba_3CeRu_2O_9$ exhibits hexagonal symmetry (space group $P6_3/mmc$) with lattice constants $a = 5.8878$ Å and $c = 14.644$ Å and intra-dimer Ru-Ru distance $d = 2.48$ Å, see Fig. 1. In $Ba_3CeRu_2O_9$, both Ce and Ru ions are tetravalent[30]. We studied single crystals with hexagonal shape and an area of about 0.45 mm × 0.4 mm perpendicular to the c axis and a thickness of roughly 0.15 mm along c.

RIXS

We performed RIXS measurements at the Ru L_3 edge in horizontal scattering geometry at beamline P01 at PETRA-III[60]. The incoming x-rays were first monochromatized by a pair of cryogenically cooled asymmetric Si(111) crystals to obtain a bandwidth of about 0.6 eV. A secondary four-bounce monochromator (asymmetric) further reduced the bandwidth to about 60 meV. We achieved an excellent total energy resolution of 64 meV by using a SiO_2 $(10\bar{2})$ diced analyzer crystal with a rectangular mask of 30 mm height. We measured at 20 K with incident π polarization and a fixed scattering angle of $2\theta = 90^\circ$, strongly suppressing elastic (Thomson) scattering. For each angle of incidence θ, the energy of zero loss was determined by measuring elastic scattering from GE varnish applied next to the sample. All RIXS data have been corrected for self-absorption effects based on the scattering geometry and the energy of the scattered photons[61], using an x-ray absorption spectrum measured at $2\theta = 90^\circ$ and $\theta = 45^\circ$ on the (001) facet.

Concerning RIXS interferometry, the fixed scattering angle of 90° yields a fixed modulus $|\mathbf{q}|$ such that we can explore the modulation pattern only by changing the orientation of $\mathbf{q}$ with respect to the dimer axis. Therefore, we studied two sample orientations. The first one uses a (110) surface with (110) and (001) lying in the scattering plane. The second sample features a (001) surface with (001) and (100) spanning the scattering plane. The sample orientation was determined by Laue diffraction and, for the sample with the (001)-(100) scattering plane, the additional observation of the (002) Bragg reflection.

Data availability

The numerical simulations of the excitation spectrum and of the RIXS intensities were performed using the Quanty package[62]. The data shown in the figures is available on Zenodo[63] https://doi.org/10.5281/zenodo.20209703.

Received: 8 April 2026; Accepted: 2 June 2026;
Published online: 13 June 2026

References

1. Khomskii, D. I. *Transition Metal Compounds* (Cambridge University Press, 2014).

2. Streltsov, S. V. & Khomskii, D. I. Orbital physics in transition metal compounds: New trends. *Phys. Usp.* **60**, 1121 (2017).
3. Khomskii, D. I. & Streltsov, S. V. Orbital effects in solids: basics, recent progress, and opportunities. *Chem. Rev.* **121**, 2992–3030 (2021).
4. Streltsov, S. V. & Khomskii, D. I. Covalent bonds against magnetism in transition metal compounds. *Proc. Natl. Acad. Sci. USA.* **113**, 10491–10496 (2016).
5. Streltsov, S. V. & Khomskii, D. I. Orbital-dependent singlet dimers and orbital-selective Peierls transitions in transition-metal compounds. *Phys. Rev. B* **89**, 161112(R) (2014).
6. Ishida, K. et al. Spin-triplet superconductivity in Sr_2RuO_4 identified by ^{17}O Knight shift. *Nature* **396**, 658–660 (1998).
7. Pustogow, A. et al. Constraints on the superconducting order parameter in Sr_2RuO_4 from oxygen-17 nuclear magnetic resonance. *Nature* **574**, 72–75 (2019).
8. Maeno, Y., Yonezawa, S. & Ramires, A. Still mystery after all these years - unconventional superconductivity of Sr_2RuO_4. *J. Phys. Soc. Jpn* **93**, 062001 (2024).
9. Nakatsuji, S., Ikeda, S.-I. & Maeno, Y. Ca_2RuO_4: New Mott insulators of layered ruthenate. *J. Phys. Soc. Jpn.* **66**, 1868 (1997).
10. Braden, M., André, G., Nakatsuji, S. & Maeno, Y. Crystal and magnetic structure of Ca_2RuO_4: Magnetoelastic coupling and the metal-insulator transition. *Phys. Rev. B* **58**, 847 (1998).
11. Anisimov, V. I., Nekrasov, I. A., Kondakov, D. E., Rice, T. M. & Sigrist, M. Orbital-selective Mott-insulator transition in $Ca_{2-x}Sr_xRuO_4$. *Eur. Phys. J. B* **25**, 191–201 (2002).
12. Neupane, M. et al. Observation of a novel orbital selective Mott transition in $Ca_{1.8}Sr_{0.2}RuO_4$. *Phys. Rev. Lett.* **103**, 097001 (2009).
13. Takahashi, H. et al. Nonmagnetic $J = 0$ state and spin-orbit excitations in K_2RuCl_6. *Phys. Rev. Lett.* **127**, 227201 (2021).
14. Kunkemöller, S. et al. Highly anisotropic magnon dispersion in Ca_2RuO_4: evidence for strong spin orbit coupling. *Phys. Rev. Lett.* **115**, 247201 (2015).
15. Jain, A. Higgs mode and its decay in a two-dimensional antiferromagnet. *Nat. Phys.* **13**, 633–637 (2017).
16. Zhang, G. & Pavarini, E. Mott transition, spin-orbit effects, and magnetism in Ca_2RuO_4. *Phys. Rev. B* **95**, 075145 (2017).
17. Gretarsson, H. et al. Observation of spin-orbit excitations and Hund's multiplets in Ca_2RuO_4. *Phys. Rev. B* **100**, 045123 (2019).
18. Sarte, P. M., Stock, C., Ortiz, B. R., Hong, K. H. & Wilson, S. D. Van Vleck excitons in Ca_2RuO_4. *Phys. Rev. B* **102**, 245119 (2020).
19. Mohapatra, S. & Singh, A. Magnetic reorientation transition in a three orbital model for Ca_2RuO_4 - interplay of spin-orbit coupling, tetragonal distortion, and Coulomb interactions. *J. Phys. Condens. Matter* **32**, 485805 (2020).
20. Feldmaier, T., Strobel, P., Schmid, M., Hansmann, P. & Daghofer, M. Excitonic magnetism at the intersection of spin-orbit coupling and crystal-field splitting. *Phys. Rev. Res.* **2**, 033201 (2020).
21. Vergara, I. et al. Spin-orbit coupling and crystal-field splitting in Ti-doped Ca_2RuO_4 studied by ellipsometry. *Phys. Rev. B* **106**, 085103 (2022).
22. Khaliullin, G. Excitonic magnetism in van Vleck-type d^4 Mott insulators. *Phys. Rev. Lett.* **111**, 197201 (2013).
23. Nikolaev, S. A., Solovyev, I. V. & Streltsov, S. V. Quantum spin liquid and cluster Mott insulator phases in the Mo_3O_8 magnets. *npj Quantum Mater.* **6**, 25 (2021).
24. Petersen, T., Bhattacharyya, P., Rößler, U. K. & Hozoi, L. Resonating holes vs molecular spin-orbit coupled states in group-5 lacunar spinels. *Nat. Commun.* **14**, 5218 (2023).
25. Chen, G. V. & Wu, C. Multiflavor Mott insulators in quantum materials and ultracold atoms. *npj Quantum Mater.* **9**, 1 (2024).
26. Jayakumar, V. & Hickey, C. Elementary building blocks for cluster Mott insulators. *Phys. Rev. B* **113**, 035151 (2026).
27. Li, Y. et al. Soft and anisotropic local moments in 4d and 5d mixed-valence M_2O_9 dimers. *Phys. Rev. B* **102**, 235142 (2020).
28. Magnaterra, M. et al. Quasimolecular $J_{tet} = 3/2$ moments in the cluster Mott insulator $GaTa_4Se_8$. *Phys. Rev. Lett.* **133**, 046501 (2024).
29. Nguyen, L. T. & Cava, R. J. Hexagonal perovskites as quantum materials. *Chem. Rev.* **121**, 2935–2965 (2021).
30. Doi, Y. et al. Crystal structures and magnetic properties of the 6*H*-perovskites $Ba_3LnRu_2O_9$ (Ln = Ce, Pr and Tb). *J. Mater. Chem.* **11**, 3135–3140 (2001).
31. Doi, Y., Matsuhira, K. & Hinatsu, Y. Crystal structures and magnetic properties of 6*H*-perovskites $Ba_3MRu_2O_9$ (M = Y, In, La, Sm, Eu, and Lu). *J. Solid State Chem.* **165**, 317–323 (2002).
32. Hinatsu, Y. & Doi, Y. Structures and magnetic properties of double perovskites A_2LnMO_6 and 6*H*-perovskites $Ba_3LnRu_2O_9$ (A = Sr, Ba; Ln = Y, Lanthanides; M = Nb, Ta, Ru). *Bull. Chem. Soc. Jpn.* **76**, 1093–1113 (2003).
33. Revelli, A. et al. Resonant inelastic x-ray incarnation of Young's double-slit experiment. *Sci. Adv.* **5**, eaav4020 (2019).
34. Revelli, A. et al. Quasimolecular electronic structure of the spin-liquid candidate $Ba_3InIr_2O_9$. *Phys. Rev. B* **106**, 155107 (2022).
35. Magnaterra, M. et al. RIXS interferometry and the role of disorder in the quantum magnet $Ba_3Ti_{3-x}Ir_xO_9$. *Phys. Rev. Res.* **5**, 013167 (2023).
36. Dey, T. et al. Persistent low-temperature spin dynamics in the mixed-valence iridate $Ba_3InIr_2O_9$. *Phys. Rev. B* **96**, 174411 (2017).
37. Kimber, S. A. J. et al. Charge order at the frontier between the molecular and solid states in $Ba_3NaRu_2O_9$. *Phys. Rev. Lett.* **108**, 217205 (2012).
38. Hayashida, S. et al. Magnetic ground state of the dimer-based hexagonal perovskite $Ba_3ZnRu_2O_9$. *Phys. Rev. B* **111**, 104418 (2025).
39. Senn, M. S., Kimber, S. A. J., Arevalo Lopez, A. M., Hill, A. H. & Attfield, J. P. Spin orders and lattice distortions of geometrically frustrated 6*H*-perovskites $Ba_3B'Ru_2O_9$ (B' = La^{3+}, Nd^{3+}, and Y^{3+}). *Phys. Rev. B* **87**, 134402 (2013).
40. Chen, Q. et al. Realization of the orbital-selective Mott state at the molecular level in $Ba_3LaRu_2O_9$. *Phys. Rev. Mater.* **4**, 064409 (2020).
41. Yuan, B. et al. Exploring a new regime of molecular orbital physics in 4*d* cluster magnets with resonant inelastic x-ray scattering. *Phys. Rev. Lett.* **134**, 106504 (2025).
42. Ziat, D. et al. Frustrated spin-1/2 molecular magnetism in the mixed-valence antiferromagnets $Ba_3MRu_2O_9$ (M = In, Y, Lu). *Phys. Rev. B* **95**, 184424 (2017).
43. Chen, Q. et al. Large positive zero-field splitting in the cluster magnet $Ba_3CeRu_2O_9$. *J. Am. Chem. Soc.* **141**, 9928–9936 (2019).
44. Magnaterra, M. et al. Quasimolecular electronic structure of the trimer iridate $Ba_4NbIr_3O_{12}$. *Phys. Rev. B* **111**, 085122 (2025).
45. Katukuri, V. M. et al. Charge ordering in Ir dimers in the ground state of $Ba_5AlIr_2O_{11}$. *Phys. Rev. B* **105**, 075114 (2022).
46. Porter, Z. et al. Spin-orbit excitons and electronic configuration of the $5d^4$ insulator $Sr_3Ir_2O_7F_2$. *Phys. Rev. B* **106**, 115140 (2022).
47. Kwon, J. et al. Intertwined orders in a quantum-entangled metal. *Nat. Mater.* **25**, 610–617 (2026).
48. Söderström, J. et al. Parity violation in resonant inelastic soft X-ray scattering at entangled core holes. *Sci. Adv.* **10**, eadk3114 (2024).
49. Bhartiya, V. K. et al. Magnetic excitations and absence of charge order in the van der Waals ferromagnet $Fe_{4.75}GeTe_2$. *npj Quantum Mater.* **10**, 80 (2025).
50. Suzuki, H. et al. Spin waves and spin-state transitions in a ruthenate high-temperature antiferromagnet. *Nat. Mater.* **18**, 563–567 (2019).
51. Streltsov, S., Mazin, I. I. & Foyevtsova, K. Localized itinerant electrons and unique magnetic properties of $SrRu_2O_6$. *Phys. Rev. B* **92**, 134408 (2015).
52. Krajewska, A. et al. Nearly linear orbital molecules on a pyrochlore lattice. *Sci. Adv.* **10**, eadn3880 (2024).
53. Warzanowski, P. et al. Electronic excitations in $5d^4$ $J = 0$ Os^{4+} halides studied by resonant inelastic x-ray scattering and optical spectroscopy. *Phys. Rev. B* **108**, 125120 (2023).

54. Khomskii, D. I., Kugel, K. I., Sboychakov, A. O. & Streltsov, S. V. Role of local geometry in the spin and orbital structure of transition metal compounds. *J. Exp. Theor. Phys.* **122**, 484–498 (2016).
55. Kugel, K. I., Khomskii, D. I., Sboychakov, A. O. & Streltsov, S. V. Spin-orbital interaction for face-sharing octahedra: Realization of a highly symmetric SU(4) model. *Phys. Rev. B* **91**, 155125 (2015).
56. Revelli, A. et al. Fingerprints of Kitaev physics in the magnetic excitations of honeycomb iridates. *Phys. Rev. Res.* **2**, 043094 (2020).
57. Magnaterra, M. et al. RIXS observation of bond-directional nearest-neighbor excitations in the Kitaev material Na_2IrO_3. Preprint at https://arxiv.org/abs/2301.08340 (2023).
58. Warzanowski, P. et al. Spin-orbit coupling in a half-filled t_{2g} shell: the case of $5d^3$ K_2ReCl_6. *Phys. Rev. B* **109**, 155149 (2024).
59. Thakur, G. S., Chattopadhyay, S., Doert, T., Herrmannsdörfer, T. & Felser, C. Crystal growth of spin-frustrated $Ba_4Nb_{0.8}Ir_{3.2}O_{12}$: a possible spin liquid material. *Cryst. Growth Des.* **20**, 2871–2876 (2020).
60. Gretarsson, H. et al. IRIXS: a resonant inelastic X-ray scattering instrument dedicated to x-rays in the intermediate energy range. *J. Synchrotron Radiat.* **27**, 538–544 (2020).
61. Minola, M. et al. Collective nature of spin excitations in superconducting cuprates probed by resonant inelastic x-ray scattering. *Phys. Rev. Lett.* **114**, 217003 (2015).
62. Haverkort, M. W. Quanty for core level spectroscopy – excitons, resonances and band excitations in time and frequency domain. *J. Phys. Conf. Ser.* **712**, 012001 (2016).
63. Pätzold, L. et al. Data for "Between Mott and cluster Mott: spin-orbit entangled dimer singlets in $Ba_3CeRu_2O_9$", https://doi.org/10.5281/zenodo.20209703 (2026).

Acknowledgements

We pay our sincere tribute to Daniel Khomskii, who has been a major source of inspiration for our work on cluster Mott insulators and beyond. We would like to acknowledge DESY – a member of the Helmholtz Association HGF – for access to beam time. Furthermore, we acknowledge funding from the Deutsche Forschungsgemeinschaft (DFG, German Research Foundation) through Project No. 277146847 – CRC 1238 (projects A02, B03), Project No. 247310070 – CRC 1143 (project A05), the Würzburg-Dresden Cluster of Excellence on Complexity and Topology in Quantum Matter – ct.qmat (EXC 2147, project-id 390858490), and by the Swedish Research Council through Project No. 2025-0409.

Author contributions

L.P., P.v.L., and M.G. conceived the experiment. H.S. and P.B. synthesized the single crystals used for the measurements. L.P., H.G., E.B. and M.G. carried out the experiment at PETRA III. L.P. and M.M. analyzed the experimental data. L.P., A.S. and M.H. performed the theoretical calculations assisted by J.v.d.B. Finally, L.P., A.S., M.H. and M.G. wrote the manuscript with contributions from all the other authors.

Funding

Open Access funding enabled and organized by Projekt DEAL.

Competing interests

The authors declare no competing interests.

Additional information

Supplementary information The online version contains supplementary material available at https://doi.org/10.1038/s41535-026-00909-0.

Correspondence and requests for materials should be addressed to Markus Grüninger.